Applied Surface Science 439 (2018) 525–532

Contents lists available at ScienceDirect

Applied Surface Science

journal homepage: www.elsevier.com/locate/apsusc

Full Length Article

# Electrically driven plasmon-exciton coupled random lasing in ZnO metal-semiconductor-metal devices

Mohammad Suja [a], Bishwajit Debnath [a], Sunayna B. Bashar [a], Longxing Su [a,b], Roger Lake [a], Jianlin Liu [a,*]

[a] Department of Electrical and Computer Engineering, University of California, Riverside, CA 92521, United States
[b] School of Physics and Engineering, Sun Yat-sen University, Guangzhou 510275, People's Republic of China

ARTICLE INFO

*Article history:*
Received 18 March 2017
Revised 17 November 2017
Accepted 8 January 2018
Available online 09 January 2018

*Keywords:*
Ag nanoparticles
Metal-semiconductor-metal
Plasmonics
Random laser
ZnO

ABSTRACT

Electrically driven plasmon-exciton coupled random lasing is demonstrated by incorporating Ag nanoparticles on Cu-doped ZnO metal-semiconductor-metal (MSM) devices. Both photoluminescence and electroluminescence studies show that emission efficiencies have been enhanced significantly due to coupling between ZnO excitons and Ag surface plasmons. With the incorporation of Ag nanoparticles on ZnO MSM structures, internal quantum efficiency up to 6 times is demonstrated. Threshold current for lasing is decreased by as much as 30% while the output power is increased up to 350% at an injection current of 40 mA. A numerical simulation study reveals that hole carriers are generated in the ZnO MSM devices from impact ionization processes for subsequent plasmon-exciton coupled lasing.



## 1. Introduction

Zinc oxide (ZnO) has been considered as one of the potential candidates for achieving ultraviolet (UV) lasers at room temperature (RT) due to a direct wide bandgap of 3.37 eV and a high exciton binding energy of 60 meV through several approaches such as, Fabry-Perot, random, and whispering-gallery mode in a variety of nanostructure systems [1–8]. Random lasing phenomenon occurs by forming random optical path through scattering in the grain boundaries of the random media, which results in random excitation of lasing modes in comparison with defined lasing modes in conventional lasers [9]. Recently, random lasers have attracted a great deal of interest thanks to its simple device structures and potential applications in various fields, in particular, speckle-free imaging and water purification [10–15]. Although ZnO-based random lasers have been demonstrated in ZnO films and nanostructures in both optical and electrical excitation [3,4,16–30], the relatively high threshold current and low output power have remained as major issues that hinder the further development of this technology into practical products.

To address these issues, p-n junctions together with double heterostructures and quantum confined structures would have been a natural direction to pursue [31,32]. Nevertheless, it is now known that although p-type conductivity can be realized in ZnO, its reliability still remains poor. Therefore, it is important to develop alternative device structures other than p-n junctions. Recently, surface plasmons (SP) have gained intensive attention due to their unique properties and applications in enhancing the emission efficiency of light emitting materials, including InGaN/GaN quantum wells, Si quantum dots (QD), CdSe QDs, and ZnO films [33–40]. However, SP-enhanced electroluminescence (EL) of ZnO-based light emitting diodes (LEDs) and laser diodes has been rarely reported to date [37–40]. In this paper, we report SP-enhanced metal-semiconductor-metal (MSM) ZnO random lasers for the first time. The MSM devices were fabricated by using gold-nickel (Au/Ni) and gold-titanium (Au/Ti) Schottky contacts onto copper (Cu)-doped ZnO thin films grown by radio-frequency (RF) plasma-assisted molecular beam epitaxy (MBE). The hole generation for lasing has been found to mainly originate from impact ionization processes using a ZnO MSM device model. Silver (Ag) nanoparticles (NPs) with different densities were incorporated on the surface of ZnO MSM devices to investigate the plasmonic enhancement. The plasmonic enhancement has been explained in terms of reduced threshold current, and enhanced internal quantum efficiency and output power, which originate from the efficient coupling between SPs in Ag NPs and excitons in ZnO.

## 2. Materials and methods

### 2.1. Cu-doped ZnO thin film growth

Cu-doped ZnO thin film was grown on *c*-sapphire substrate in a SVTA (SVT Associates, Inc.) RF plasma-assisted MBE system.

* Corresponding author.
*E-mail address:* jianlin@ece.ucr.edu (J. Liu).

https://doi.org/10.1016/j.apsusc.2018.01.075
0169-4332/

Knudsen effusion cells filled with high-purity elemental Zn (6N), Mg (6N), and Cu (6N) were used as Zn, Mg and Cu sources, and $O_2$ (6N) gas was fed through a RF plasma generator as the O source. The substrate was cleaned in an aqua regia ($HNO_3$:HCl = 1:3) solution at 150 °C for 40 min, rinsed in deionized (DI) water, blown dry using a nitrogen gun, transferred to the MBE system, and annealed in vacuum at 800 °C for 15 min to produce an atomically clean surface. A low-temperature MgO/ZnO (~3 nm/8 nm) buffer layer was grown at a substrate temperature of 450 °C, an Mg cell temperature of 450 °C, a Zn cell temperature of 320 °C, and an $O_2$ flow rate of 2 sccm with a plasma power of 400 W. Then a thick ZnO (~400 nm) buffer layer was deposited for 3 h at a substrate temperature of 400 °C, a Zn cell temperature of 320 °C, and an $O_2$ flow rate of 1.75 sccm, respectively. Next, while all the growth conditions were kept the same as that for the ZnO buffer, the shutter of a Cu effusion cell at a temperature of 750 °C was opened and the growth lasted for 2 h, leading to a Cu-doped ZnO layer of ~280 nm. Finally, the film was *in situ* annealed at 700 °C for 20 min under $O_2$ environment with an $O_2$ flow rate of 2.5 sccm. The total thickness of the film is about 700 nm. The as grown film is designated as Sample 1.

### 2.2. Ag NPs incorporation

Ag NPs incorporation was carried out using two different ways and total three samples were prepared. For Sample 2, commercially purchased Ag colloids (20 nm, Ted Pella, Inc.) were spin-coated (1500 rpm for 15 s) on the surface of the ZnO:Cu film and then annealed at 150 °C for 2 min. This process was repeated 5 times to increase the density of Ag NPs. For Sample 3 and 4, Ag NPs were self-assembled by e-beam evaporation of Ag with a thickness of 1 Å (Sample 3) and 2 Å (Sample 4) on the ZnO:Cu film at a rate of 0.1 Å/s in a Temescal BJD 1800 e-beam evaporator, followed by a rapid thermal annealing (RTA) at 500 °C for 60 s.

### 2.3. Structural, optical and electrical characterizations

The thickness of the film was measured by a Veeco systems Dektak 8 surface profilometer. A Bruker D8 Advance X-ray diffractometer was used to perform X-ray diffraction (XRD) measurement. X-ray photoelectron spectroscopy (XPS) characterization was carried out by using a Kratos Axis Ultra DLD XPS system equipped with an Al Kα monochromated X-ray source and a 165-mm mean radius electron energy hemispherical analyzer. Scanning electron microscope (SEM) images were captured by a Philips XL-30 SEM machine. SEM images were taken using an acceleration voltage of 10 kV and a secondary electron detector. Photoluminescence (PL) measurements were carried out using a home-built PL system consisting of a Kimmon Koha 325-nm He-Cd laser excitation source, an Oriel monochromator, a photomultiplier detector, a lock-in amplifier, a chopper and a Janis cryostat with a Cryocon 22 temperature controller. A Varian Cary 500 double-beam scanning ultraviolet/visible/near-infrared (UV/vis/NIR) spectrophotometer was used for absorption measurements. For Hall effect measurements, a Keithley 6220 current source and a Keithley 2182 voltmeter were used with minimum current capability of 0.1 pA with up to 105 V compliance and voltage capability of 1 nV, respectively. Au/Ti (100 nm/10 nm) was deposited by e-beam evaporation for Hall bar geometry sample as metal contact and followed by a RTA annealing.

### 2.4. MSM random laser device fabrication and characterization

MSM random laser devices were fabricated using standard photolithography process. The outer circular ring contact area has an outer and inner diameter of 450 μm and 400 μm, respectively. The inner crossbar contact has an inner circle of diameter 100 μm with four elongated cross rectangular section (100 μm × 20 μm). Au/Ni (150 nm/20 nm) and Au/Ti (150 nm/20 nm) were deposited by e-beam evaporation on the ZnO:Cu layer as inner crossbar and outer circular contact metals for the M(Au/Ni)-S(ZnO:Cu)-M(Au/Ti) structure, respectively. The current-voltage (I-V) characteristics were measured using an Agilent 4155C semiconductor parameter analyzer. MSM random laser devices were packaged on TO5 cans for electroluminescence (EL) measurements. EL spectra were collected using the same home-built system as PL. An external HP E3630A dc power supply was used to inject current to the devices. Output power of the devices was measured using a Thorlabs PM100 optical power meter.

### 2.5. MSM random laser device simulation

A 3D semiconductor model has been simulated to understand the electrostatic properties of Cu-doped ZnO MSM device using Finite Element (FE) analysis simulation tool, COMSOL [41]. A 700-nm *c*-grown ZnO layer serves as the core of the model, with an assumption of no surface trap states and defect sites. The ZnO layer is assumed to have an electron carrier concentration of $9 \times 10^{15}$ $cm^{-3}$, which is selected to be in line with the experimental results. The bulk *c*-sapphire ($Al_2O_3$) substrate was effectively modeled as an insulating boundary. The Au/Ni and Au/Ti form two Schottky barriers with ZnO because of the difference in their electron affinities [42]. Since the Schottky barrier height is small (0.3–0.5 V), the device turn-on is rather fast, which is also consistent with observed experimental I-V curve. We used Fermi-Dirac statistics to describe the behavior of both majority (electron) and minority (hole) carriers. The electron mobility is 30 $cm^2/V$ s, whereas the hole mobility is assumed to be very low (0.1–1 $cm^2/V$ s) [43]. An iterative non-linear solver is adopted to solve the coupled drift-diffusion, carrier continuity, Poisson, and thermionic emission equations in COMSOL.

To understand the origin of electroluminescence, we have simulated the hole concentration in a 2D ZnO channel using impact ionization model, as implemented in ATLAS [44]. The conventional drift-diffusion model cannot capture the non-local effect such as kinetic energy gain by electrons from high electric field, as well as energy lost to the lattice due to electron-lattice collision [45]. Hence, rather than relying on the local electric field, the carrier energy distribution (*i.e.*, carrier temperature) is used to calculate an effective non-local field, which describes the impact ionization process more accurately [46]. The carrier temperature is determined from the linearized Boltzmann transport equation, assuming a Maxwellian shape to the distribution of hot carriers [47]. The hot electrons subsequently cause impact ionization in the space-charge region of the reverse-biased junction. The electric field ($E_{eff}$) dependence of the impact generation coefficient is described by $\alpha_{ZnO} = A \exp\left[-\left(\frac{B}{E_{eff}}\right)\right]$ [48,49], where $A = 7 \times 10^5$ $cm^{-1}$, $B = 5 \times 10^6$ V/cm are the extracted material parameters calculated from the ionization rate reported for ZnO [50]. The saturation velocity for electrons in ZnO is taken as $\sim 3 \times 10^7$ cm/s [51], and the relaxation time is assumed to be 1.5 ps [52].

## 3. Results

### 3.1. Structural characterizations

Fig. 1(a) shows an XRD spectrum of the Cu-doped ZnO film (Sample 1). The spectrum exhibits diffraction peaks of ZnO (0002) at ~34.4° and $Al_2O_3$ (0006) at ~41.6°, indicating that ZnO has grown preferentially along *c*-direction of the wurtzite lattice structure. Fig. 1(b) shows XPS spectrum of as grown Cu-doped

ZnO film, showing Zn 2p and O 1s core level spectra. In the range of Zn 2p orbital peak, two distinct peaks at binding energies of 1021 eV and 1044 eV corresponding to Zn $2p_{3/2}$ and Zn $2p_{1/2}$, respectively can be observed. The binding energy difference between these two states is around 23 eV, which lies within the standard reference value of ZnO [53]. The O 1s peak is centered at 529.8 eV, which is attributed to $O^{2-}$ ions on the wurtzite structure of the hexagonal $Zn^{2+}$ ion array, surrounded by Zn atoms [54]. Inset of Fig. 1(b) shows the high resolution Cu 2p core level spectrum displaying peaks at 933.2 eV and 953 eV corresponding to Cu $2p_{3/2}$ and Cu $2p_{1/2}$, respectively. This result indicates that Cu dopant exists in the form of copper (I) oxide ($Cu^{+1}$) in the film [55].

Fig. 2(a) shows an SEM image of the ZnO:Cu film (Sample 1). The film possesses grains and air gaps, which facilitate the formation of random lasing cavities in the active layer. This morphology originates from a low-quality buffer layer and a relatively low-temperature growth of active layer on a lattice mismatched sapphire substrate. Inset shows a cross-sectional SEM image of the sample, indicating that the film is continuous and relatively uniform. Fig. 2(b) shows an SEM image of the ZnO:Cu film with spin-coated Ag NPs (Sample 2). The size of the Ag NPs is 25–35 nm and the density is $\sim 4.8 \times 10^9\ cm^{-2}$. Fig. 2(c) and (d) show SEM images of Sample 3 and 4, respectively. These self-assembled Ag NPs were formed by e-beam evaporation and subsequent annealing (Methods section). The size and density of Ag NPs in Sample 3 are 15–25 nm and $\sim 1.6 \times 10^{10}\ cm^{-2}$, respectively, while the size and density of Ag NPs in Sample 4 are 35–45 nm and $\sim 1.8 \times 10^{10}\ cm^{-2}$, respectively.

### 3.2. Optical characterizations

Fig. 3(a) shows RT PL spectra of the four samples. The near band edge (NBE) emission peaks at 380 nm are observed for all samples and PL enhancement is evident after Ag NPs are incorporated on ZnO:Cu films. Compared with the sample without Ag NPs (Sample 1), the NBE peak enhancement ratio is about 4 for Sample 2, and increases to 5 for Sample 3 as the density of Ag NPs increases. The enhancement ratio is 2 for Sample 4 as both the size and density of Ag NPs reach the highest values compared to other samples. A slightly enhanced green emission peak is observed at around 500 nm for Sample 2, which can be attributed to some defects induced by the colloids of commercially purchased Ag NPs. Inset of Fig. 3(a) shows NBE PL enhancement ratio with respect to the density of Ag NPs. The non-monotonous trend suggests that the plasmon coupling efficiency reflected in the enhancement ratio clearly correlates the density of Ag NPs.

Fig. 3(b) shows absorption spectra of the samples. All spectra exhibit strong absorption in the spectrum region below 380 nm, and are almost transparent over 390 nm. The samples with incorporated Ag NPs show an absorption enhancement around 400 nm due to the excitation of localized surface plasmon modes in the Ag NPs. The absorption spectrum of Ag colloidal NPs exhibits an absorption band centered at 400 nm (Fig. S1, Supporting Information), which can be attributed to the surface plasmon resonance (SPR) absorption of Ag NPs. Since the absorption band of Ag NPs overlaps with the ZnO NBE emission spectrum, the emission from the ZnO MSM devices can be enhanced resonantly by the surface plasmons of Ag NPs [39].

### 3.3. Electrical characterizations

Electrical properties of the Cu-doped ZnO films with and without Ag NPs are summarized in Fig. S2 and Table S1. Fig. S2 shows Hall resistance as a function of magnetic field at room temperature for all samples. The negative sloped lines represent the n-type conductivity of the samples. As seen from Table S1, all samples show a carrier concentration in the range of $1–4 \times 10^{15}\ cm^{-3}$, mobility of $17–32\ cm^2\ V^{-1}\ s^{-1}$ and resistivity of 80–140 Ω cm. Since Cu is a p-type dopant for ZnO [55], the incorporation of Cu atoms in the present ZnO film was not enough to make it p-type, nevertheless, these acceptors still heavily compensate unintentional donors, leading to the observed relative low electron carrier concentration and mobility. This low electron carrier concentration is desired for facilitating the formation of Schottky junctions instead of Ohmic junctions for lasing [56].

Fig. 4(a) shows a schematic of ZnO MSM random laser devices with and without Ag NPs. As-deposited Au/Ni and Au/Ti serve as two contacts of the MSM device. I-V characteristics are shown in both linear and semi-log scale (inset) in Fig. 4(b) for ZnO MSM devices with and without Ag NPs. The almost symmetric behavior of these I-V curves under forward (positive voltage on Au/Ni contact) and reverse biases indicates typical characteristic of MSM device [57,58]. The similarity in the electrical properties and I-V curves indicate that the incorporation of discrete Ag NPs does not alter the electrical properties. This implies that the optical emission enhancement is triggered due to plasmonic effect rather than any change in carrier modification.

### 3.4. Lasing characteristics

Fig. 5(a) shows EL spectra of ZnO:Cu MSM device without Ag NPs (Sample 1). The spectra were recorded from the top surface

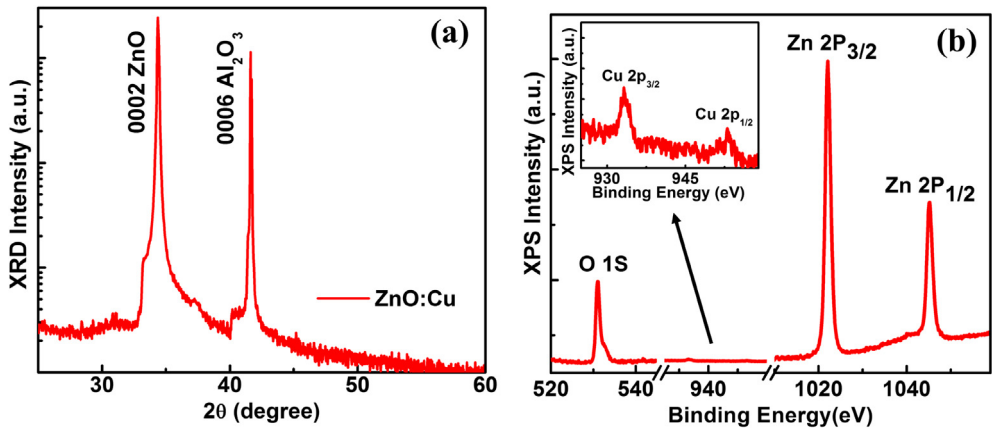


**Fig. 1.** (a) XRD spectrum of Cu-doped ZnO thin film, (b) Zn 2p and O 1s core level XPS spectra, inset showing Cu 2p core level XPS spectrum.

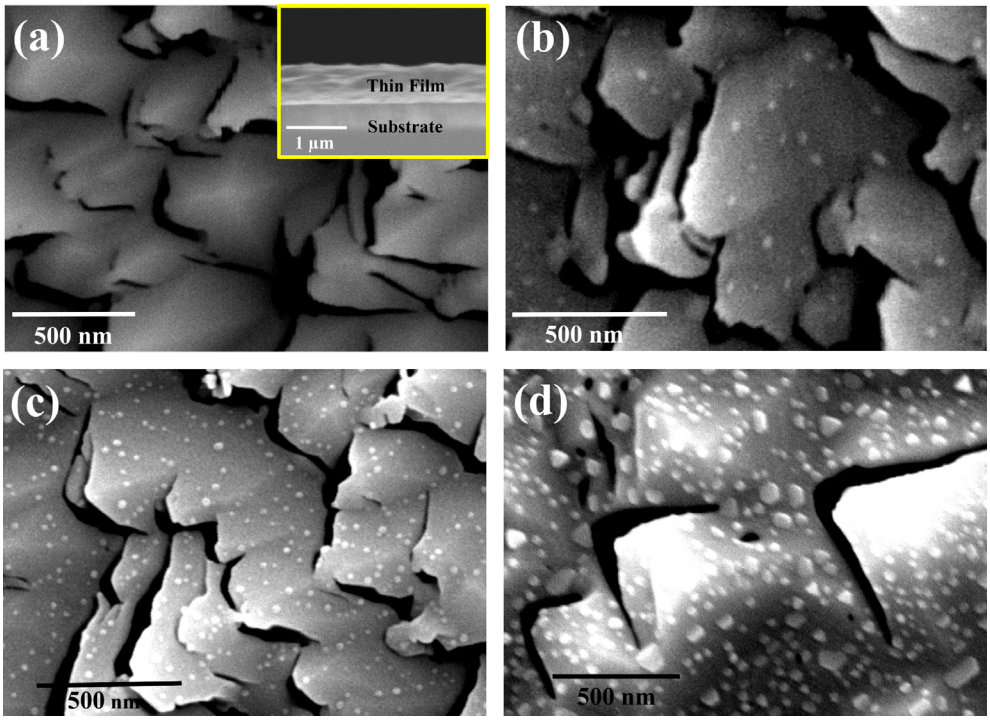


**Fig. 2.** (a) SEM image of Cu-doped ZnO thin film (Sample 1), inset shows cross sectional view SEM image of the film, (b) SEM image of Sample 2, (c) SEM image of Sample 3, (d) SEM image of Sample 4.

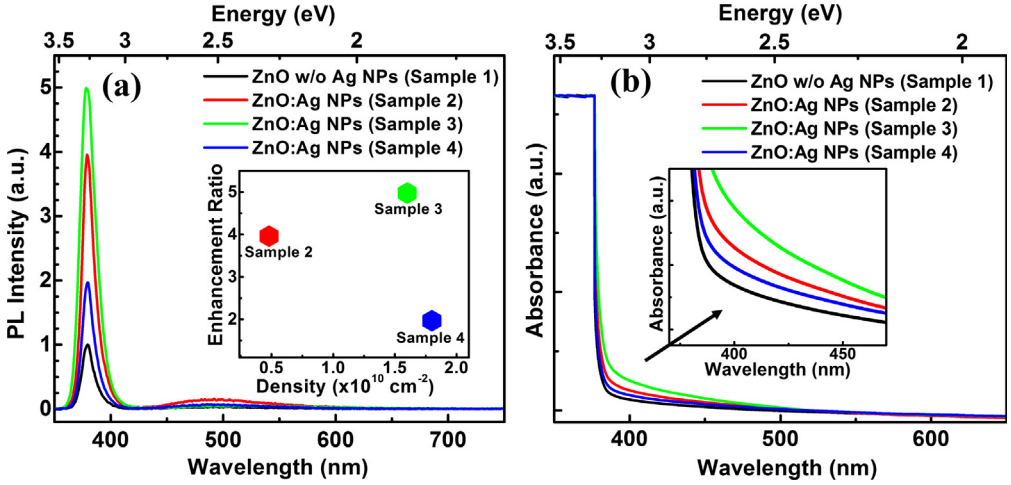


**Fig. 3.** (a) RT photoluminescence spectra of ZnO films without (Sample 1) and with (Samples 2–4) Ag NPs, (b) Absorption spectra of ZnO films without (Sample 1) and with (Samples 2–4) Ag NPs.

of Sample 1 at different dc injection currents under positive biases applied on the Au/Ni contact with respect to Au/Ti contact at room temperature. The same procedure was used to collect emission spectra for other samples. At lower injection currents less than 28 mA, a broad spontaneous emission peak is observed at around 380 nm, which can be attributed to the NBE emission of ZnO. As the injection current increases to about 31 mA, narrow peaks with a full width at half maximum (FWHM) of around 1.5–2 nm become visible at around 380 nm. Multiple narrow peaks emerge randomly between 370 nm and 400 nm with stronger intensity as the injection current increases further. The inset of Fig. 5(a) shows the integrated emission intensity and output power as a function of injection current. The integrated emission intensity is an integral of the area under the emission spectra representing an output from all emission wavelengths. The output power was obtained by real time measurement at the strongest lasing mode near 380 nm. As seen from the graph, an output power of about 40 nW is detected at an injection current of 40 mA. Both data show similar trend, deducing a threshold current of about 30 mA.

Fig. 5(b)–(d) show EL spectra of Ag NPs incorporated ZnO:Cu MSM random laser devices (Samples 2–4). For Sample 2, a broad spontaneous emission is centered around 388 nm at an injection current of 18 mA. With higher injection currents, stimulated emission peaks with a FWHM of about 0.5 nm become superimposed on the broad spontaneous emission peak. Inset of Fig. 5(b) shows integrated emission intensity and measured output power as a function of injection current of the device. The threshold current decreases to 20 mA (a 30% decrease compared to that of Sample

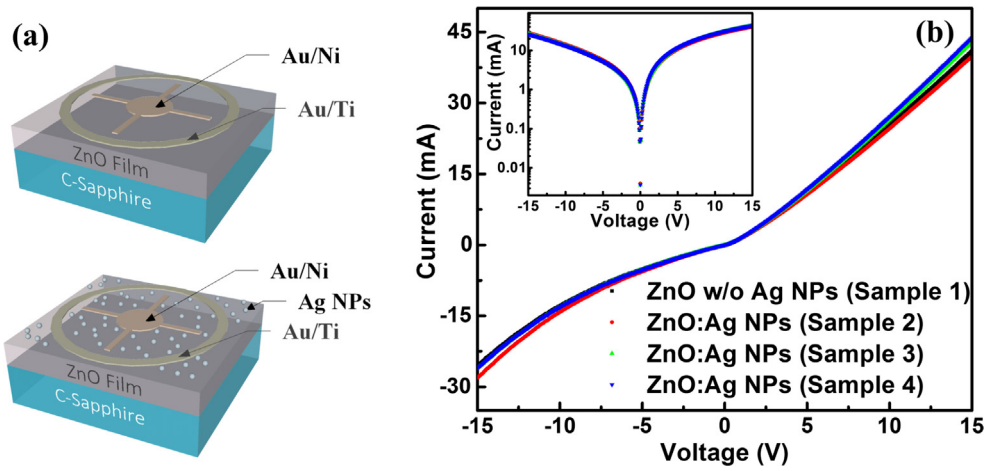


**Fig. 4.** (a) Schematic of MSM random laser devices with (bottom) and without (top) Ag NPs, (b) I-V characteristics in linear scale of MSM devices (Samples 1–4), inset shows the semi-log scale.

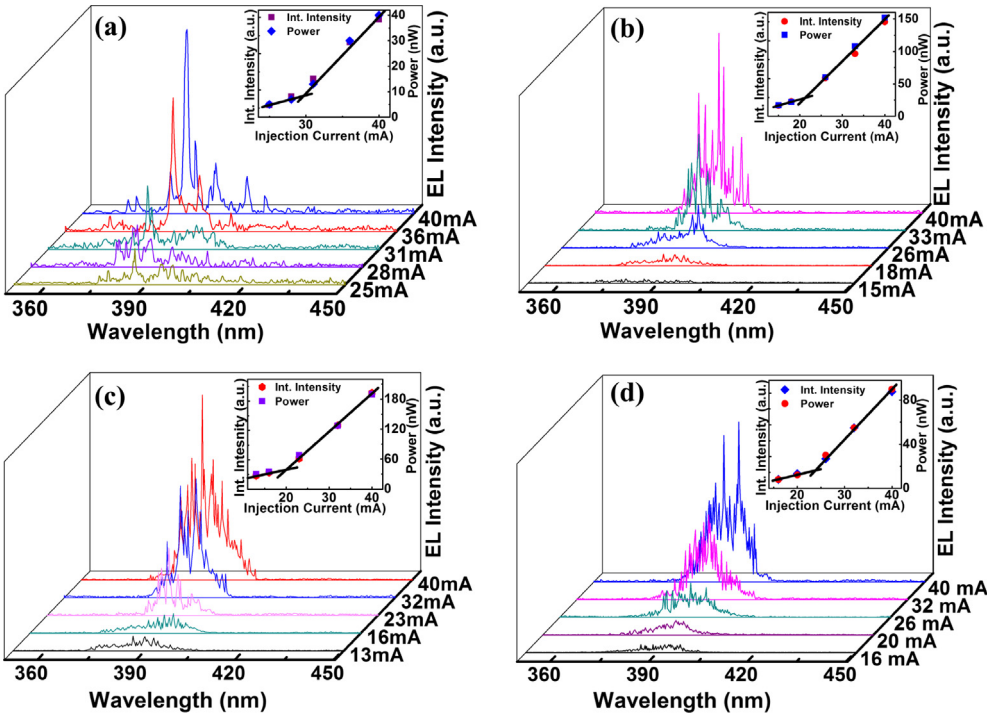


**Fig. 5.** RT electroluminescence spectra from (a) Sample 1, (b) Sample 2, (c) Sample 3, and (d) Sample 4, under different injection current. Inset shows integrated intensity and output power as a function of injection current.

1) while the output power increases to 150 nW at the same injection current of 40 mA after incorporating Ag NPs on the ZnO:Cu MSM device (Sample 2). For Sample 3, a broad spontaneous emission peak is visible around 390 nm at an injection current of 16 mA. As the injection current increases, more and more stimulated emission peaks with a FWHM of about 0.3–0.5 nm emerging on top of the spontaneous emission peak. The threshold current is also about 20 mA for Sample 3 while the power increases to 180 nW (the increase is 350% compared to that of Sample 1) at an injection current of 40 mA as shown in the inset of Fig. 5(c). Having the highest density of Ag NPs among these samples, Sample 4 shows similar broad spontaneous emission peak centered around 390 nm at lower injection currents and stimulated emissions (a FWHM of 0.3–0.5 nm) superimpose on the spontaneous emission at higher injection currents. The threshold current of about 26 mA is evident for Sample 4 and an output power of 80 nW was recorded at an injection current of 40 mA as depicted in the inset of Fig. 5(d). Further comparison of EL spectra of samples with and without Ag NPs leads to the fact that both spontaneous and stimulated emissions are enhanced due to plasmonic effect.

To compare the EL enhancement effect by the deposition of Ag nanoparticles, Fig. S3(a) in the Supporting Information shows EL emission spectra of Samples 1–4 at the same injection current of 40 mA. Compared with Sample 1, both spontaneous emission and stimulated emission are enhanced under this current for Samples 2–4. Fig. S3(b) (Supporting Information) shows integrated intensity ratio of Sample 2–4 with respect to Sample 1 as a function of injection current. The emission intensity enhancement is clearly observed, in particular at higher injection levels, for example, the ratio is 4.04, 6.64, and 3.07 for Samples 2–4, respectively at an

injection current of 40 mA. At the same injection level below threshold, the spontaneous emission enhancement is also observed for the samples with Ag nanoparticles, which generally agrees with the PL results.

## 4. Discussion

Finally, we discuss the mechanism of plasmon-exciton coupled lasing behavior from Ag-NP-coated ZnO:Cu MSM random laser devices. Although the majority carriers (electrons) control the transport in the ZnO MSM devices, the experimental observation of luminescence indicates the presence of minority carriers (holes). We can roughly estimate a lower bound number of electron-hole pairs necessary for radiative recombination at a particular lasing wavelength by the equation, $P_{out} = \frac{n}{t} \times h\nu$, where, $h\nu$ is the photon energy. For ZnO:Cu MSM random laser device (Sample 1), the measured output power, $P_{out} = 40$ nW at ~15 V [Fig. 5(a) inset]. So the number of holes per second $(n/t)$ responsible for recombination is in the range of $\sim 7 \times 10^{10}$ cm$^{-3}$/s. Considering the photons from both stimulated and spontaneous emissions at other wavelengths and also additional non-radiative recombination, the total hole supply rate could be much higher than this rough estimation.

To understand how the holes are generated in these ZnO MSM devices, first, finite element simulation tool COMSOL Multiphysics was used to simulate electrical statistics of these devices (see Methods section and similar approach in dealing with MgZnO devices [59]). Fig. 6(a) and (b) show band diagrams of an MSM device with a 50-μm ZnO channel terminated by Au/Ni and Au/Ti metal contacts in thermal equilibrium and under a positive bias of 15 V, respectively. Under applied positive bias on the Au/Ni contact, almost all the potential drops in the depletion region of Au/Ti/ZnO Schottky junction, resulting in a localized high field region. The electron can accelerate in the field region and gain energy to create electron-hole pairs (EHP) by impact ionization. Then, a non-local impact ionization model in an Atlas simulation tool was used to simulate the hole generation and steady state excess hole concentration (see Methods section for details). Fig. 6(c) shows hole concentration as a function of position between Au/Ni and Au/Ti contacts. The generation of holes are confined only at the space charge region near the reverse-biased Schottky junction (outer Au/Ti contact in this case). As the applied bias increases, the hole generation increases. The highest steady-state excess hole concentration reaches $10^8$–$10^9$ cm$^{-3}$ at a bias of ~15 V. Due to a high exciton binding energy of 60 meV in ZnO, the excess holes will have ample probabilities to instantaneously interact with electrons to form excitons, which can recombine radiatively to generate excitonic emission [60]. The generated photons scatter randomly at the grain boundaries with air gaps in the thin film to form the close-loop cavities for random lasing [32].

The Ag NPs are essentially nanoscale antennas that can radiate electromagnetic energy [61,62]. Since the exciton energies in ZnO:Cu are similar to the electron oscillation energy of localized surface plasmon modes in Ag, the exciton energies can be coupled to the SP modes of Ag NPs due to the direct contact of these NPs with ZnO. In literature [33–40,61–65], several approaches were used to recover the energies from the SP modes into free space as emitted light including the introduction of grating structures of a right period and the roughening of the sample surface because these approaches enable the surface plasmon modes to have non-zero component of their wave vectors along the normal direction, which is an important criterion for the evanescent plasmonic modes to be scattered into free space. The surface of our random lasers is inherently rough, thus these exciton energies can be extracted as light in this alternative emission path in addition to usual photon emission path from the surface of the ZnO:Cu layer [37]. It is expected that with Ag NPs on the surface, the light output and external quantum efficiency are enhanced. The external quantum efficiency is equal to the product of light extraction factor and internal quantum efficiency ($\eta_{int}$), and the $\eta_{int}$ can be described as

$$\eta_{int} = \frac{R_{rad}}{R_{rad} + R_{non}},$$

where $R_{rad}$ and $R_{non}$ are the radiative and non-radiative recombination rates of electron-hole pairs (EHPs) in ZnO, respectively. The internal quantum efficiency ($\eta'_{int}$) of the ZnO with exciton-SP coupling can be described as

$$\eta'_{int} = \frac{R_{rad} + C'_{ext}R_{LSP}}{R_{rad} + R_{non} + R_{LSP}},$$

where $C'_{ext}$ is the probability of photon extraction from the generated SP's energy and $R_{LSP}$ is the exciton-SP coupling rate [35]. The exciton-SP coupling rate is much faster than the radiative and non-radiative rates [37], leading to enhanced internal quantum efficiency ($\eta'_{int}$). Temperature-dependent PL spectra of these samples are shown in Fig. S4 (Supporting Information), from which the integrated PL intensities can be estimated to extract the internal quantum efficiencies. Assuming $\eta_{int} \approx 100\%$ at 13 K for all samples, $\eta_{int}$ can be estimated as 0.36% from the plot for ZnO:Cu without Ag NPs at room temperature [66]. After the incorporation of Ag NPs, the internal quantum efficiency increases 4.58 times ($\eta'_{int} = 1.65\%$) for Sample 2, 5.83 times ($\eta'_{int} = 2.1\%$) for Sample 3, and 2.02 times ($\eta'_{int} = 0.73\%$) for Sample 4, respectively. The enhanced internal quantum efficiencies can be construed as the increased spontaneous

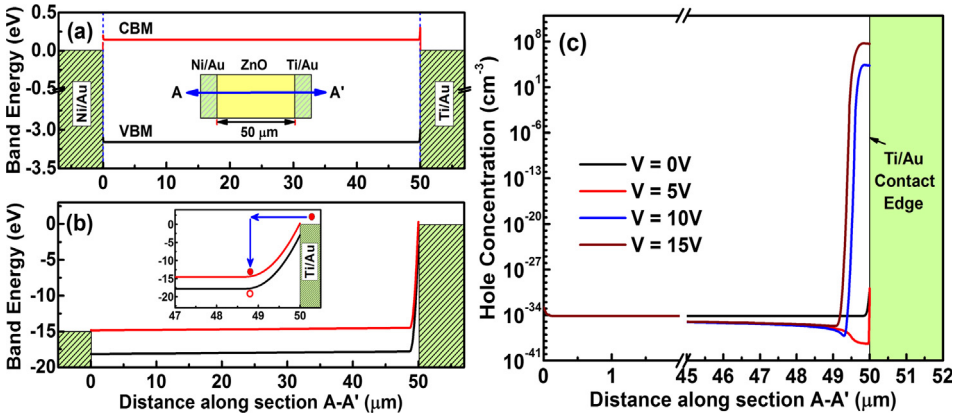


**Fig. 6.** Band diagram of ZnO along A–A′ section direction for (a) V = 0 V and (b) V = 15 V. The inset shows a closer view in the SC region and explains the impact ionization process by hot electrons, (c) Hole concentration along A–A′ section, calculated from non-local impact ionization model.

recombination rates as a result of the exciton-SP coupling, which further enhances the light emission efficiency.

To reassure that the samples undergo the exciton-SP coupling process during lasing operation, we can calculate the lasing threshold carrier density of all samples and compare with the Mott density. The carrier density Δn can be estimated by: $J = \frac{q\Delta n}{\tau} d$, where J is the current density, q is fundamental charge, d = 700 nm is the total thickness of gain medium of the devices, and $\tau = \eta_{int}\tau_r$ is the total recombination time. The internal quantum efficiency $\eta_{int}$ is estimated through PL, and radiative recombination time $\tau_r$ = 0.97 ns is taken from literature [67]. The threshold current density was estimated in the EL measurements to be 15.87–23.8 A/cm$^2$ for Sample 1–4. Thus, threshold carrier density can be calculated, $\Delta n = 4.96 \times 10^{12}$ cm$^{-3}$ for Sample 1, $2.27 \times 10^{13}$ cm$^{-3}$ for Sample 2, $2.83 \times 10^{13}$ cm$^{-3}$ for Sample 3 and $9.92 \times 10^{12}$ cm$^{-3}$ for Sample 4. Obviously, all these numbers are much smaller than the Mott density of around $10^{17}$ cm$^{-3}$ in ZnO [68]. This result suggests that the present lasing is indeed under excitonic regime rather than electron-hole plasma type and with the addition of Ag nanoparticles, efficient exciton-plasmon coupling leads to the enhanced emission.

## 5. Conclusion

Plasmon-enhanced ZnO MSM random laser devices were fabricated and studied. After the incorporation of Ag NPs on ZnO:Cu MSM devices, the efficient coupling of Ag SPs and ZnO excitons leads to the decrease of lasing threshold current by 30% and the increase of the output power by 350%. In addition, an increase of internal quantum efficiency by six times was observed. A numerical simulation of the ZnO MSM devices suggests that the supply of holes for lasing is originated from impact ionization process under relatively high voltages. This unique technique of employing surface plasmons to couple with excitons could lead to a new era of low-threshold semiconductor lasers.

## Acknowledgements

This work was supported by SHINES, an Energy Frontier Research Center funded by the US Department of Energy, Office of Science, Basic Energy Sciences under Award #SC0012670.

## Appendix A. Supplementary material

Supplementary data associated with this article can be found, in the online version, at https://doi.org/10.1016/j.apsusc.2018.01.075.

## References

[1] D.M. Bagnall, Y.F. Chen, Z. Zhu, T. Yao, S. Koyama, M.Y. Shen, T. Goto, Optically pumped lasing of ZnO at room temperature, Appl. Phys. Lett. 70 (1997) 2230–2232.
[2] S. Chu, G.P. Wang, G.P. Zhou, Y.Q. Lin, L. Chernyak, J.Z. Zhao, J.Y. Kong, L. Li, J.J. Ren, J.L. Liu, Electrically pumped waveguide lasing from ZnO nanowires, Nat. Nanotechnol. 6 (2011) 506–510.
[3] S.F. Yu, S.P. Lau, W.I. Park, G.C. Yi, Random laser action in ZnO nanorod arrays embedded in ZnO epilayers, Appl. Phys. Lett. 84 (2004) 3241–3243.
[4] H. Cao, Y.G. Zhao, S.T. Ho, E.W. Seelig, Q.H. Wang, R.P.H. Chang, Random laser action in semiconductor powder, Phys. Rev. Lett. 82 (1999) 2278–2281.
[5] J.H. Choy, E.S. Jang, J.H. Won, J.H. Chung, D.J. Jang, Y.W. Kim, Soft solution route to directionally grown ZnO nanorod arrays on Si wafer; room-temperature ultraviolet laser, Adv. Mater. 15 (2003) 1911–1914.
[6] C. Czekalla, C. Sturm, R.D. Schmidt-Grund, B. Cao, M. Lorenz, M. Grundmann, Whispering gallery mode lasing in zinc oxide microwires, Appl. Phys. Lett. 92 (2008) 241102.
[7] J. Dai, C.X. Xu, K. Zheng, C.G. Lv, Y.P. Cui, Whispering gallery-mode lasing in ZnO microrods at room temperature, Appl. Phys. Lett. 95 (2009) 241110.
[8] R. Chen, B. Ling, X.W. Sun, H.D. Sun, Room temperature excitonic whispering gallery mode lasing from high-quality hexagonal ZnO microdisks, Adv. Mater. 23 (2011) 2199–2204.
[9] B. Redding, M.A. Choma, H. Cao, Speckle-free laser imaging using random laser illumination, Nat. Photonics 6 (2012) 355–359.
[10] D.S. Wiersma, S. Cavalieri, Light emission: a temperature-tunable random laser, Nature 414 (2001) 708–709.
[11] R.C. Polson, Z.V. Varden, Random lasing in human tissues, Appl. Phys. Lett. 85 (2004) 1289–1291.
[12] R. Choe, A. Corlu, K. Lee, T. Durduran, S.D. Konecky, M. Grosicka-Koptyra, S.R. Arridge, B.J. Czerniecki, D.L. Fraker, A. DeMichele, B. Chance, M.A. Rosen, A.G. Yodh, Diffuse optical tomography of breast cancer during neoadjuvant chemotherapy: a case study with comparison to MRI, Med. Phys. 32 (2005) 1128–1139.
[13] D.S. Wiersma, The physics and applications of random lasers, Nat. Phys. 4 (2008) 359–367.
[14] Q. Song, S. Xiao, Z. Xu, V.M. Shalaev, Y.L. Kim, Random laser spectroscopy for nanoscale perturbation sensing, Opt. Lett. 35 (2010) 2624–2626.
[15] Q. Song, Z. Xu, S.H. Choi, X. Sun, S. Xiao, O. Akkus, Y.L. Kim, Detection of nanoscale structural changes in bone using random lasers, Biomed. Opt. Express 1 (2010) 1401–1407.
[16] N.M. Lawandy, R.M. Balachandran, A.S.L. Gomes, E. Sauvain, Laser action in strongly scattering media, Nature 368 (1994) 436–438.
[17] H.D. Li, S.F. Yu, S.P. Lau, E.S.P. Leong, Simultaneous formation of visible and ultraviolet random lasings in ZnO films, Appl. Phys. Lett. 89 (2006) 021110.
[18] H. Yan, J. Johnson, M. Law, R. He, K. Knutsen, J.R. McKinney, J. Pham, R. Saykally, P. Yang, ZnO Nanoribbon microcavity lasers, Adv. Mater. 15 (2003) 1907–1911.
[19] H.C. Hsu, C.Y. Wu, W.F. Hsieh, Stimulated emission and lasing of random-growth oriented ZnO nanowires, J. Appl. Phys. 97 (2005) 064315.
[20] X. Ma, J. Pan, P. Chen, D. Li, H. Zhang, Y. Yang, D. Yang, Room temperature electrically pumped ultraviolet random lasing from ZnO nanorod arrays on Si, Opt. Express 17 (2009) 14426–14433.
[21] Y.T. Chen, Y.F. Chen, Enhanced random lasing in ZnO nanocombs assisted by fabry-perot resonance, Opt. Express 19 (2011) 8728–8734.
[22] C.H. Liu, J.A. Zapien, Y. Yao, X.M. Meng, C.S. Lee, S.S. Fan, Y. Lifshitz, S.T. Lee, High-density, ordered ultraviolet light-emitting ZnO nanowire arrays, Adv. Mater. 15 (2003) 838–841.
[23] E.S. Leong, S.F. Yu, UV random lasing action in p-SiC(4H)/i-ZnO–SiO2 nanocomposite/n-ZnO: Al heterojunction diodes, Adv. Mater. 18 (2006) 1685–1688.
[24] J. Huang, S. Chu, J.Y. Kong, L. Zhang, C.M. Schwarz, G.P. Wang, L. Chernyak, Z.H. Chen, J.L. Liu, ZnO p–n homojunction random laser diode based on nitrogen-doped p-type nanowires, Adv. Opt. Mater. 1 (2013) 179–185.
[25] S.B. Bashar, M. Suja, M. Morshed, F. Gao, J. Liu, An Sb-doped p-type ZnO nanowire based random laser diode, Nanotechnology 27 (2016) 065204.
[26] F. Gao, M.M. Morshed, S.B. Bashar, Y. Zheng, Y. Shi, J. Liu, Electrically pumped random lasing based on an Au–ZnO nanowire Schottky junction, Nanoscale 7 (2015) 9505–9509.
[27] Y.J. Lu, C.X. Shan, M.M. Jiang, G.C. Hu, N. Zhang, S.P. Wang, B.H. Li, D.Z. Shen, Random lasing realized in n-ZnO/p-MgZnO core–shell nanowire heterostructures, Cryst. Eng. Comm. 17 (2015) 3917–3922.
[28] S. Bashar, M. Suja, W. Shi, J. Liu, Enhanced random lasing from distributed Bragg reflector assisted Au-ZnO nanowire Schottky diode, Appl. Phys. Lett. 109 (2016) 192101.
[29] X.Y. Liu, C.X. Shan, S.P. Wang, Z.Z. Zhang, D.Z. Shen, Electrically pumped random lasers fabricated from ZnO nanowire arrays, Nanoscale 4 (2012) 2843–2846.
[30] C.Y. Liu, H.Y. Xu, J.G. Ma, X.H. Li, X.T. Zhang, Y.C. Liu, R. Mu, Electrically pumped near-ultraviolet lasing from ZnO/MgO core/shell nanowires, Appl. Phys. Lett. 99 (2011) 063115.
[31] S. Chu, J.H. Lim, L.J. Mandalapu, Z. Yang, L. Li, J.L. Liu, Sb-doped p-ZnO/Ga-doped n-ZnO homojunction ultraviolet light emitting diodes, Appl. Phys. Lett. 92 (2008) 152103.
[32] J. Kong, S. Chu, Z. Zuo, J. Ren, M. Olmedo, J. Liu, Low-threshold ZnO random lasing in a homojunction diode with embedded double heterostructure, Appl. Phys. A 107 (2012) 971.
[33] J.S. Biteen, N.S. Lewis, H.A. Atwater, H. Mertens, A. Polman, Spectral tuning of plasmon-enhanced silicon quantum dot luminescence, Appl. Phys. Lett. 88 (2006) 131109.
[34] K. Okamoto, S. Vyawahare, A. Scherer, Surface-plasmon enhanced bright emission from CdSe quantum-dot nanocrystals, J. Opt. Soc. Am. B 23 (2006) 1674–1678.
[35] K. Okamoto, I. Niki, A. Shvartser, Y. Narukawa, T. Mukai, A. Scherer, Surface-plasmon-enhanced light emitters based on InGaN quantum wells, Nat. Mater. 3 (2004) 601–605.
[36] C.W. Lai, J. An, H.C. Ong, Surface-plasmon-mediated emission from metal-capped ZnO thin films, Appl. Phys. Lett. 86 (2005) 251105.
[37] S.G. Zhang, X.W. Zhang, Z.G. Yin, J.X. Wang, J.J. Dong, H.L. Gao, F.T. Si, S.S. Sun, Y. Tao, Localized surface plasmon-enhanced electroluminescence from ZnO-based heterojunction light-emitting diodes, Appl. Phys. Lett. 99 (2011) 181116.
[38] H. Shen, C.X. Shan, Q. Qiao, J.S. Liu, B.H. Li, D.Z. Shen, Stable surface plasmon enhanced ZnO homojunction light-emitting devices, J. Mater. Chem. C 1 (2013) 234–237.
[39] Q. Qiao, C.X. Shan, J. Zheng, H. Zhu, S.F. Yu, B.H. Li, Y. Jia, D.Z. Shen, Surface plasmon enhanced electrically pumped random lasers, Nanoscale 5 (2013) 513–517.

[40] Q. Qiao, C.X. Shan, J. Zheng, B.H. Li, Z.Z. Zhang, D.Z. Shen, Surface plasmon enhanced ultraviolet light-emitting devices, J. Lumin. 134 (2013) 754–757.
[41] COMSOL, Semiconductor Module, COMSOL Inc., 2016.
[42] K. Ip, G.T. Thalera, H. Yang, S.Y. Han, Y. Li, D.P. Norton, S.J. Pearton, S. Jang, F. Ren, Contacts to ZnO, J. Cryst. Growth 287 (2006) 149–156.
[43] D.C. Look, D.C. Reynolds, C.W. Litton, R.L. Jones, D.B. Eason, G. Cantwell, Characterization of homoepitaxial p-type ZnO grown by molecular beam epitaxy, Appl. Phys. Lett. 81 (2002) 1830.
[44] ATLAS, Device Simulator, Atlas, Silvaco International, Santa Clara, CA.
[45] R. Stratton, Diffusion of hot and cold electrons in semiconductor barriers, Phys. Rev. 126 (1962) 2002.
[46] T. Grasser, T.W. Tang, H. Kosina, S. Selberherr, A review of hydrodynamic and energy-transport models for semiconductor device simulation, Proc. IEEE 91 (2003) 251.
[47] K. Katayama, T. Toyabe, A new hot carrier simulation method based on full 3D hydrodynamic equations, Electron Devices Meeting, IEDM '89. Technical Digest. International, 1989, pp. 135–138.
[48] S. Selberherr, Analysis and Simulation of Semiconductor Devices, Springer, 1984.
[49] Y. Okuto, C.R. Crowell, Threshold energy effect on avalanche breakdown voltage in semiconductor junctions, Solid State Electron. 18 (1975) 161–168.
[50] F. Bertazzi, M. Goano, E. Bellotti, Electron and hole transport in bulk ZnO: a full band monte carlo study, J. Electron. Mater. 36 (2007) 857–863.
[51] J.D. Albrecht, P.P. Ruden, S. Limpijumnong, W.R.L. Lambrecht, K.F. Brennan, High field electron transport properties of bulk ZnO, J. Appl. Phys. 86 (1999) 6864.
[52] E. Šermukšnis, J. Liberis, M. Ramonas, A. Matulionis, M. Toporkov, H.Y. Liu, V. Avrutin, Ü. Özgür, H. Morkoç, Hot-electron energy relaxation time in Ga-doped ZnO films, J. Appl. Phys. 117 (2015) 065704.
[53] C.D. Wagner, W.M. Riggs, L.E. Davis, J.F. Moulder, G.E. Muilenberg, Handbook of X-ray Photoelectron Spectroscopy, Perkin Elmer, Eden Prairie, 1979.
[54] J.C.C. Fan, J.B. Goodenough, X-ray photoemission spectroscopy studies of Sn-doped indium-oxide films, J. Appl. Phys. 48 (1977) 3524.
[55] M. Suja, S.B. Bashar, M.M. Morshed, J.L. Liu, Realization of Cu-doped p-type ZnO thin films by molecular beam epitaxy, ACS Appl. Mater. Interfaces 7 (2015) 8894–8899.
[56] M.M. Morshed, M. Suja, Z. Zuo, J. Liu, Ultraviolet random lasing from asymmetrically contacted MgZnO metal-semiconductor-metal device, Appl. Phys. Lett. 105 (2014) 211107.
[57] K. Liu, M. Sakurai, M. Aono, ZnO-based ultraviolet photodetectors, Sensors 10 (2010) 8604–8634.
[58] L.J. Mandalapu, F.X. Xiu, Z. Yang, J.L. Liu, Al/Ti contacts to Sb-doped p-ZnO, J. Appl. Phys. 102 (2007) 023716.
[59] M. Suja, S.B. Bashar, B. Debnath, L.X. Su, W.H. Shi, R. Lake, J.L. Liu, Electrically driven deep ultraviolet MgZnO lasers at room temperature, Sci. Rep. 7 (2017) 2677.
[60] H. Jeong, K. Min, S. Byun, C.J. Stanton, D.H. Reitze, J.K. Yoo, G.C. Yi, Y.D. Jho, Excitonic diffusion dynamics in ZnO, Appl. Phys. Lett. 100 (2012) 092106.
[61] J. Cesario, M. Gonzalez, S. Cheylan, W. Barnes, S. Enoch, R. Quidant, Coupling localized and extended plasmons to improve the light extraction through metal films, Opt. Express 15 (2007) 10533–10539.
[62] X. Gu, T. Qiu, W. Zhang, P. Chu, Light-emitting diodes enhanced by localized surface plasmon resonance, Nanoscale Res. Lett. 6 (2011) 199.
[63] X.H. Xiao, F. Ren, X.D. Zhou, T.C. Peng, W. Wu, X.N. Peng, X.F. Yu, C.Z. Jiang, Surface plasmon-enhanced light emission using silver nanoparticles embedded in ZnO, Appl. Phys. Lett. 97 (2010) 071909.
[64] P. Cheng, D. Li, Z. Yuan, P. Chen, D. Yang, Enhancement of ZnO light emission via coupling with localized surface plasmon of Ag island film, Appl. Phys. Lett. 92 (2008) 041119.
[65] T. Nakamura, S. Sonoda, S. Adachi, Plasmonic control of ZnO random lasing characteristics, Laser Phys. Lett. 11 (2014) 016004.
[66] Y. Kawakami, K. Omae, A. Kaneta, K. Okamoto, T. Izumi, S. Sajou, K. Inoue, Y. Narukawa, T. Mukai, Sg. Fujita, Radiative and nonradiative recombination processes in GaN-based semiconductors, Phys. Status Solidi A 183 (2001) 41–50.
[67] T. Koida, S.F. Chichibu, A. Uedono, A. Tsukazaki, M. Kawasaki, T. Sota, Y. Segawa, H. Koinuma, Correlation between the photoluminescence lifetime and defect density in bulk and epitaxial ZnO, Appl. Phys. Lett. 82 (2003) 532.
[68] C. Klingshirn, R. Hauschild, J. Fallert, H. Kalt, Room-temperature stimulated emission of ZnO: alternatives to excitonic lasing, Phys. Rev. B 75 (2007) 115203.